

# Detection of small targets in the infrared: an infrared search and track tutorial

RONALD DRIGGERS,<sup>1,\*</sup> EYTAN POLLAK,<sup>2</sup> ROBERT GRIMMING,<sup>3</sup>  ECTIS VELAZQUEZ,<sup>2</sup> ROBERT SHORT,<sup>3</sup> GERALD HOLST,<sup>4</sup> AND ORGES FURXHI<sup>5</sup>

<sup>1</sup>Wyatt College of Optical Sciences, University of Arizona, Tucson, Arizona 85721, USA

<sup>2</sup>L3Harris, Orlando, Florida 32816, USA

<sup>3</sup>University of Central Florida, Orlando, Florida 32816, USA

<sup>4</sup>JCD Publishing Co., Oviedo, Florida 32765, USA

<sup>5</sup>Imec USA Nanoelectronics Design Center, Kissimmee, Florida 34744, USA

\*Corresponding author: rdriggers@arizona.edu

Received 12 March 2021; revised 30 April 2021; accepted 1 May 2021; posted 3 May 2021 (Doc. ID 424767); published 27 May 2021

Airborne target detection in the infrared has been classically known as infrared search and track or IRST. From a military point of view, it can be described as target detection at long ranges where the target image is subpixel in size. Here, the target is “unresolved.” It can also describe the detection of aircraft near the observer using distributed apertures in a spherical detection field. From a commercial point of view, an important application is drone detection near live airport operations. As drones become more common, the dual-use functionality of IRST systems is expanding. Technology improvements for IRST systems include the wide proliferation of infrared staring focal planes. New readout integrated circuits allow for time-delay-integration of large format detectors. Stare-step sensors in the future appear to be as common as gimbal-scanned thermal imagers. Detection probability analysis and IRST sensor design is different than targeting system design. We provide a tutorial here on IRST system calculations as well as discussions on broadband versus spectral calculations and new technology considerations. © 2021 Optical Society of America

<https://doi.org/10.1364/AO.424767>

## 1. INTRODUCTION

Infrared search and track (IRST) systems detect and locate far away airborne targets. Usually the target angular extent is less than the sensor instantaneous field of view (IFOV). This is called “unresolved” target acquisition. Currently, there are three widely utilized applications for IRST systems.

The first application is detection of enemy aircraft at significantly long ranges. These high-performance systems are used when radar and/or electronic warfare equipment is jammed, compromised, or simply turned off. These systems have large apertures, narrow field of view (FOV) and scanned detectors. With a large field of regard (FOR), the revisit rate is low. Figure 1 illustrates a typical mounted system. The second application is incoming missile warning and relatively close enemy aircraft location. It consists of several sensors (also called a distributed aperture system) that, in combination, provide  $2\pi$  steradians of angular coverage. The F-35 sensor provides a detection bubble around the aircraft and even allows the pilot to see through the aircraft (e.g., the glass cockpit). The third IRST application is the detection of small unmanned aerial systems (UAS; popularly called drones). As drones continue to proliferate in both commercial and military systems, detection as well as drone defense is becoming much more important. For example, between 19

and 21 December 2018, London’s Gatwick Airport was closed down due to drone sightings [1,2]; 140,000 passengers and 1000 flights were affected.

Current programs will identify and demonstrate technology solutions supporting the development of a future airborne long-range offensive IRST capability based on staring (nonscanned) system configurations. The newer staring arrays will support all IRST applications from long-range aircraft detection to



**Fig. 1.** Air Force F-16 Legion Pod IRST [3]. Similar sensors are embedded on the SAAB Gripen, the Eurofighter Typhoon, and Dassault’s Rafale.

distributed aperture system short-range aircraft detection to ground-based unmanned drones. Staring arrays have their own challenges in that the development of large format staring arrays that can cover the entire FOR are currently not feasible for large aperture systems, so scanning or stare stepping the focal plane may be required.

This paper provides a tutorial on the performance prediction ofIRST systems [3–9]. We begin this tutorial with a description of aIRST system to include scanning (second-generation thermal imaging), staring, stare stepped, and dither. We follow the description with a radiometric analysis and signal transfer of the target and background. The signal of an unresolved target (target image smaller than a detector) is characterized by the pulse visibility factor (PVF). The random location of the target image with respect to the detector grid results in a variable signal. Noise components include signal shot noise, dark current shot noise, and readout noise. Newer readout integrated circuits (ROICs) have no limits on the amount of charge storage that can be collected. The noise equivalent irradiance (NEI) metric completely describes the target/background signal at the sensor's entrance aperture. It is up to the designer to fabricate a sensor capable of detecting the NEI. We describe typical targets and how targets can be represented in the signal chain.

We provide a broadband signal-to-noise ratio (SNR) example that is common with mostIRST designs. The broadband approach requires values averaged over the spectral region of interest. The spectral NEI (SNEI) is appropriate for signals, atmospheres, and sensors that have spectral features. We describe the optimization of sensor design in terms of diffraction-limited optics coupled to detector size/pitch. The results of the optimization are realized in a comparison of scanned versus staringIRST systems. Finally, we discuss limitations in the performance of staringIRST systems and some suggestions for design rules as well as technology challenges for the future.

## 2. IRST SYSTEMS

Figure 2 illustrates the complexity of signal analysis. An aircraft is shown to the left whose signature is characterized by an intensity  $I(\lambda)$  in  $\text{W}/\text{sr}\cdot\mu\text{m}$  and target area  $A_{\text{tgt}}$  in square centimeters ( $\text{cm}^2$ ). TheIRST sensor not only senses the aircraft flux but also the background path radiance of the sky  $L_{\text{bg}}$  ( $\text{W}/\text{sr}\cdot\text{m}^2$ ) as well as the path radiance between the sensor and the target  $L_{\text{path}}$  ( $\text{W}/\text{sr}\cdot\text{m}^2$ ). The target intensity passes through

the atmospheric path between the sensor and the aircraft with an atmospheric transmission  $\tau_{\text{atm}}$  ( $\mu\text{m}$ ). The reduced intensity is converted to an irradiance on the entrance aperture of theIRST sensor in  $\text{W}/\text{cm}^2\cdot\mu\text{m}$ . The flux is reduced by the sensor optical transmission and is focused onto the focal plane array. The resulting electronic signal is a function of the image size and its location with respect to the focal plane array grid. Maximum signal occurs when the image is centered on a single detector and at a minimum when it is positioned at the corner of four detectors. This variation is described by the pulse visibility factor (PVF) (discussed in Section 4). The signals from the target and background can be quite large, whereas target detection depends upon the difference, which can be quite small. This complex analysis is significantly reduced with resolved targets (image much larger than several detectors). Here the target and background are characterized by a differential temperature, and Planck's blackbody equation provides the spectral features.

The sensors are sensitive in the longwave infrared (LWIR) or midwave infrared (MWIR) spectral regions. The detectors are mercury cadmium telluride (MCT) or indium antimonide (InSb), respectively. It is likely that InSb will be replaced with type II superlattice quantum engineered MWIR detectors.

As indicated in Fig. 2, the various signals have units of power (W), whereas modern staring arrays convert photons into electrons. Using the Planck equation, we can convert watts to photons per second and integrate over the detector quantum efficiency to produce electrons per second. This rate coupled to the detector integration time determines how many electrons are collected for both the differential target signal as well as the electrons associated with the background flux of the sky. In many cases, the noise of theIRST sensor is "background limited," sometimes called background-limited photodetection (BLIP). In this case, the background radiance of the sky and/or clouds fills most of the detector charge well. The associated shot noise is the dominant noise term. In the non-BLIP case, the detector dark current shot noise and readout noise become important. The SNR is the ratio of the differential signal to the root of all the noise electrons. While  $\text{SNR} = 1$  has become a standard mathematical threshold, it is difficult to actually detect the signal without sophisticated algorithms. It is more reasonable to select  $6 < \text{SNR} < 10$  as a detection threshold.

Figure 3 illustrates fourIRST architectures. The first is a scanned linear or time-delay-integration (TDI) array where a gimbal scans the array across the FOR. With TDI, the detector outputs are combined from each line to increase the signal

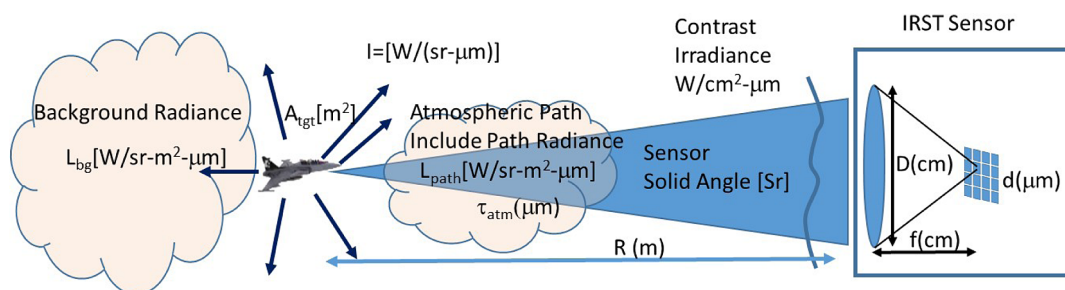


**Fig. 2.** Components considered in infrared search and track analysis. The background of the airborne target is usually open sky and/or clouds. The background is assumed to be at the same location as the target. MODTRAN provides sky background path radiance for different atmospheric types, clouds, visibility, and other conditions. Not considered here is that the background could be ground or a mountain.

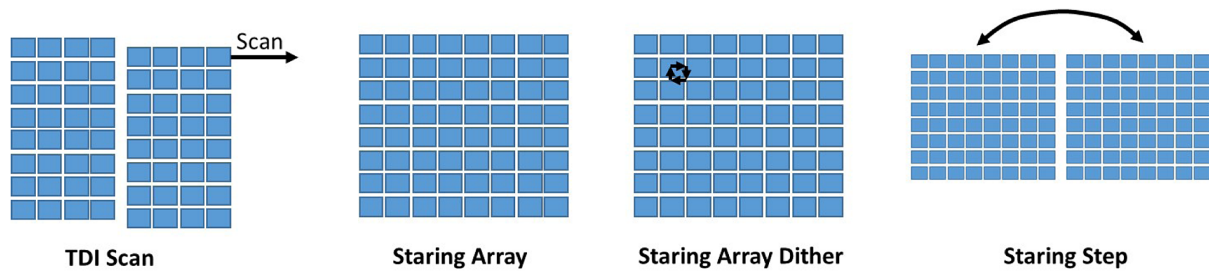


Fig. 3. IRST focal plane/system architectures.

compared to the noise in the same manner as second-generation thermal imagers [10]. The second architecture is a basic staring focal plane system that is not scanned. It should be noted that there are some systems where a full two-dimensional focal plane is scanned in a TDI fashion, but we consider that a severe case of the first architecture. Simple staring array performance is limited since a reasonable FOR means a short focal length, resulting in a small aperture (we will discuss this in detail later). One way to improve sampling is to dither (third architecture), which is useful when you are sampling limited. The IRST function is primarily sensitivity limited, not so much resolution limited, so a larger aperture is usually more important than higher resolution sampling (note that dithering can increase the number of pixels on the target depending on the unresolved target size). Finally, one method that achieves a larger aperture is stare step, where a staring focal plane takes a frame and a stare-step mirror or gimbal moves the FOV over to cover the entire FOR. From a performance perspective, this is like scanning. Since the FOV is smaller, it means that a larger aperture can be used. The relative performance of these different architectures is discussed in Section 12.

### 3. SIGNAL RADIOMETRY

We will derive the signal radiometry in two ways, broadband and spectral, as both are used frequently. From Fig. 2, the target intensity may be provided directly, or the target radiance may be provided, from which an intensity is calculated. The broadband target intensity is

$$I_{\text{tgt}} = L_{\text{tgt}} A_{\text{tgt}} \frac{\text{W}}{\text{sr}}, \quad (1a)$$

and the spectral target intensity is

$$I_{\text{tgt}}(\lambda) = L_{\text{tgt}}(\lambda) A_{\text{tgt}} \frac{\text{W}}{\text{sr} \cdot \mu\text{m}}. \quad (1b)$$

The target radiance  $L_{\text{tgt}}$  has units of  $\text{W}/\text{cm}^2\text{-sr}$  or  $\text{W}/\text{cm}^2\text{-sr} \cdot \mu\text{m}$ , respectively. The IRST sensor receives the “differential intensity,” which is manifested in the difference between a pixel detecting the target and the background and a pixel detecting only the background. For unresolved targets, as is the case for IRST, the differential intensity is simply the difference of the radiances from an area occupied by the size of the target. The rest of the area of the projected pixel contains background radiance and it cancels out. The atmospheric pedestal of sky background is usually specified in terms of path radiance.

Converting this pedestal to an equivalent intensity occupied by the size of the target, the broadband target differential intensity is

$$\Delta I_{\text{tgt}} = L_{\text{tgt}} A_{\text{tgt}} - L_{\text{bg}} A_{\text{tgt}} \frac{\text{W}}{\text{sr}}, \quad (2a)$$

and the spectral target differential intensity is

$$\Delta I_{\text{tgt}}(\lambda) = L_{\text{tgt}}(\lambda) A_{\text{tgt}} - L_{\text{bg}}(\lambda) A_{\text{tgt}} \frac{\text{W}}{\text{sr} \cdot \mu\text{m}}, \quad (2b)$$

where  $L_{\text{bg}}$  is the background radiance with units of  $\text{W}/\text{cm}^2\text{-sr}$  or  $\text{W}/\text{cm}^2\text{-sr} \cdot \mu\text{m}$ , respectively. Since the solid angle of the receiving aperture of the sensor as seen from the target is  $\Omega_{\text{sensor}} = \pi D^2 / 4R^2$ , the broadband differential power entering the aperture is

$$\Delta P_{\text{tgt}} = \frac{\pi D^2 A_{\text{tgt}}}{4R^2} [L_{\text{tgt}} - L_{\text{bg}}] \text{W}, \quad (3a)$$

and the spectral differential target power is

$$\Delta P_{\text{tgt}}(\lambda) = \frac{\pi D^2 A_{\text{tgt}}}{4R^2} [L_{\text{tgt}}(\lambda) - L_{\text{bg}}(\lambda)] \frac{\text{W}}{\mu\text{m}}. \quad (3b)$$

Adding the atmospheric transmission and path radiance provides the broadband differential target power [Eq. (4a)] and spectral differential target power [Eq. (4b)]. If the path radiance is the same for the target and background, it cancels in the equations. Although path radiance does not affect the differential signal, the path radiance photogenerated electrons fills the charge wells and contributes to shot noise:

$$\begin{aligned} \Delta P_{\text{tgt}} &= \frac{\pi D^2 A_{\text{tgt}} \tau_{\text{atm}}}{4R^2} [(L_{\text{tgt}} + L_{\text{path}}) - (L_{\text{bg}} + L_{\text{path}})] \\ &= \frac{\pi D^2 A_{\text{tgt}} \tau_{\text{atm}}}{4R^2} [L_{\text{tgt}} - L_{\text{bg}}] \text{W}, \end{aligned} \quad (4a)$$

$$\begin{aligned} \Delta P_{\text{tgt}}(\lambda) &= \frac{\pi D^2 A_{\text{tgt}} \tau_{\text{atm}}(\lambda)}{4R^2} [(L_{\text{tgt}}(\lambda) + L_{\text{path}}(\lambda)) \\ &\quad - (L_{\text{bg}}(\lambda) + L_{\text{path}}(\lambda))] \\ &= \frac{\pi D^2 A_{\text{tgt}} \tau_{\text{atm}}(\lambda)}{4R^2} [L_{\text{tgt}}(\lambda) - L_{\text{bg}}(\lambda)] \frac{\text{W}}{\mu\text{m}}. \end{aligned} \quad (4b)$$

There is an important quantity that is used with targets and backgrounds that corresponds to the differential target *irradiance* at the entrance aperture of the sensor. It is used with the

sensor NEI to calculate the SNR. This quantity is simply the differential power entering the aperture divided by the aperture area. The broadband differential target irradiance is

$$\Delta E_{\text{tgt}} = \frac{A_{\text{tgt}} \tau_{\text{atm}}}{R^2} [L_{\text{tgt}} - L_{\text{bg}}] \frac{\text{W}}{\text{cm}^2}, \quad (5a)$$

and the spectral differential target irradiance is

$$\Delta E_{\text{tgt}}(\lambda) = \frac{A_{\text{tgt}} \tau_{\text{atm}}(\lambda)}{R^2} [L_{\text{tgt}}(\lambda) - L_{\text{bg}}(\lambda)] \frac{\text{W}}{\text{cm}^2 \cdot \mu\text{m}}. \quad (5b)$$

When the target angular subtense is much smaller than a detector instantaneous field of view (IFOV), there is still a blur spot on the detector focal plane. The blur is due to diffraction and optical aberrations. The target image may fall in the center of the detector, in between two detectors, or even in the corner of four adjoining detectors. The amount of power on each detector varies dramatically based on the size of the blur spot and its location of the target image. This variation is incorporated into the PVF.

#### 4. PULSE VISIBILITY FACTOR

The PVF ( $0 \leq \text{PVF} \leq 1$ ) is an efficiency quantity that describes how much of the optical blur spot flux falls on a detector. The optical spot can be small compared to a detector, match the detector well, or be much larger than a detector. For diffraction-limited optics,  $F\lambda/d_{\text{cc}}$  is a good metric to describe how big the optical spot is compared to the detector size (we assume a 100% fill factor array).  $F$  is the  $f$ -number,  $\lambda$  is the wavelength in micrometers, and  $d_{\text{cc}}$  is the detector pitch in micrometers. If the spot is too small, the SNR is dominated by the background signal shot noise. If the spot is much bigger than a detector, the flux spills over onto many adjacent detectors, reducing the SNR. For years, IRST systems were said to be optimized with an Airy disc [11] size that provided 63% of its energy on the detector when the spot was centered [Fig. 4(a)]. The rationale behind the optimization approach was that a smaller spot could be accompanied by a smaller detector (with less noise since detector size contributes to noise). A spot much larger than a detector reduced the SNR since power was spreading over the other detectors. A spot closely matching the detector size (i.e., 63% power on a centered detector) provided for the highest SNR. Olsen *et al.* [12] showed that optimization of an IRST system

occurs with an  $F\lambda/d_{\text{cc}}$  of around 1.1–1.2 based on the average SNR instead of a centered-detector flux percentage.

The PVF not only takes into account the optical spot size compared to the detector, it can also take into account the position of the optical spot on the detector array. In Fig. 4(a), the spot is centered on a detector. The energy or flux on this spot-centered detector is called “ensquared energy.” The PVF with the spot centered on the detector is the ensquared energy (again, for many years an ensquared energy of 0.63 was optimal). The worst-case SNR occurs in Fig. 4(b) where the spot lands on the corner and the flux is dispersed over at least four detectors and possibly beyond. Instead of using the best case (ensquared energy) and the worst case, some engineers use an average PVF that provides an average SNR, even though the SNR can be higher and lower than that of the average estimate. The average PVF corresponding to the average SNR occurs by integrating the flux of a spot in a Monte Carlo simulation, where SNR is determined for a large sampling of random target positions. Then the average PVF is determined from the SNR estimates. Figure 4(c) shows a focal plane with an 80% fill factor. The ensquared energy, worst-case PVF, and average PVF decrease as the fill factor decreases.

When  $F\lambda/d_{\text{cc}}$  is small, then the spot is small on a detector, so the entire flux from the spot is collected by the detector (Fig. 5). As the spot becomes larger (larger  $F\lambda/d_{\text{cc}}$ ), the energy spills over on the adjacent detectors, even though the spot is centered. The “bump” in the blue curve is due to the first diffraction ring of the Airy disk passing between detectors. On the worst-case PVF (corner), a small spot will be divided equally by four detectors and  $\text{PVF} = 0.25$ . As the spot becomes larger, the PVF eventually reduces due to the spot covering more detectors. The green curve shows the average PVF for the large collection of random spot locations. Note that even though the green is the average PVF, the actual signal can range between the blue and the red curves.

A curve fit to the average PVF for 100% fill factor provides

$$\text{PVF} = 0.0335 + 0.9665e^{-0.887\left(\frac{F\lambda}{d_{\text{cc}}}\right)} \text{ unitless}. \quad (6)$$

While most focal planes are nearly 100% fill factor, the PVF at lower fill factors can be found in Butrimas *et al.* [13].

Historically, the PVF was not considered in NEI equations. From here on, we include the PVF. To be consistent with older literature, simply insert PVF in those equations. The PVF and

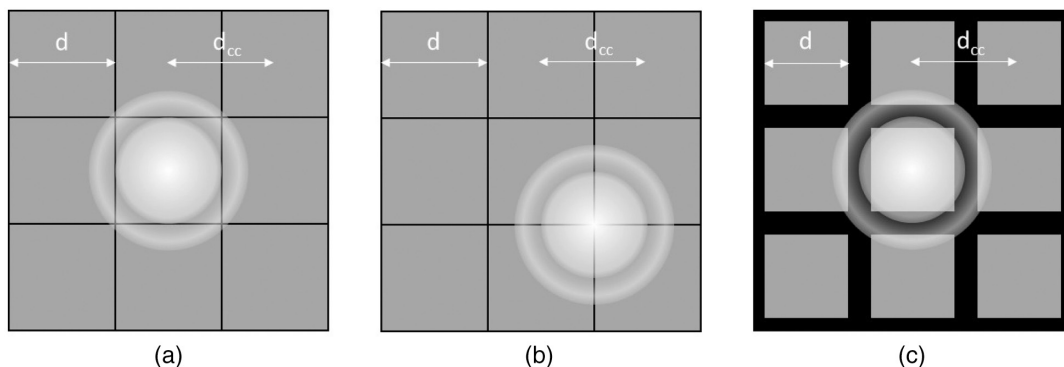


**Fig. 4.** Possible locations of a diffraction-limited spot [central lobe (Airy disc) and first ring] with respect to the array grid. (a) Ensquared energy; (b) worst-case corner location; (c) focal plane with 80% fill factor.

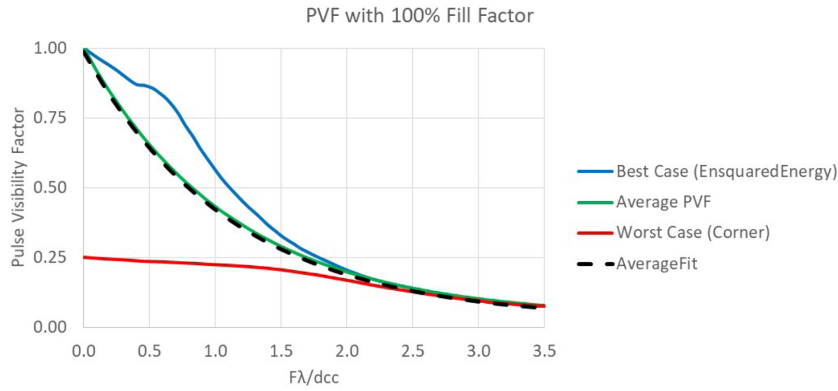


**Fig. 5.** PVF for 100% fill factor detector array.

optics transmission reduces the signal reaching the focal plane detector. Equation (4a) becomes

$$\Delta P_{\text{tgt}} = \frac{\pi D^2 A_{\text{tgt}} \tau_{\text{atm}} \tau_{\text{optics}} \text{PVF}}{4R^2} [L_{\text{tgt}} - L_{\text{bg}}] W, \quad (7a)$$

and Eq. (4b) becomes

$$\Delta P_{\text{tgt}}(\lambda) = \frac{\pi D^2 A_{\text{tgt}} \tau_{\text{atm}}(\lambda) \tau_{\text{optics}}(\lambda) \text{PVF}(\lambda)}{4R^2} \times [L_{\text{tgt}}(\lambda) - L_{\text{bg}}(\lambda)] \frac{W}{\mu\text{m}}. \quad (7b)$$

Staring array quantum efficiency is provided as electrons per photon. If all the variables in Eq. (7) have units of photons per second, it is straightforward to calculate the resultant number of electrons. Unfortunately, the target intensity is almost always provided in watts per steradian. We must convert watts to photons per second. Using Planck–Einstein’s relationship,  $E = hc/\lambda$ , where  $E$  is the energy of a photon in joules ( $J = W \cdot s$ ),  $h$  is Planck constant of  $6.626 \times 10^{-34}$  J-s,  $c$  is the speed of light at  $3 \times 10^8$  m/s, and  $\lambda$  is wavelength in meters. The broadband differential target power is

$$\Delta P_{\text{tgt}} = \frac{\pi D^2 A_{\text{tgt}} \tau_{\text{atm}} \tau_{\text{optics}} \text{PVF}}{4R^2} [L_{\text{tgt}} - L_{\text{bg}}] \frac{\lambda_{\text{ave}}}{hc} \frac{\text{photons}}{s}, \quad (8a)$$

where  $\lambda_{\text{ave}}$  is the band averaged wavelength and the spectral differential target power is

$$\Delta P_{\text{tgt}}(\lambda) = \frac{\pi D^2 A_{\text{tgt}} \tau_{\text{atm}}(\lambda) \tau_{\text{optics}}(\lambda) \text{PVF}(\lambda)}{4R^2} \times [L_{\text{tgt}}(\lambda) - L_{\text{bg}}(\lambda)] \frac{\lambda}{hc} \frac{\text{photons}}{s \cdot \mu}. \quad (8b)$$

If the target radiance and background radiance are given in photons per second, then the  $\lambda_{\text{ave}}/hc$  factor can be omitted. The average wavelength is sometimes weighted over the target and background radiance. Adding the quantum efficiency (QE) provides the number of electrons. For the broadband differential target, the number of electrons created during an integration time of  $\tau_{\text{int}}$  is

$$\Delta n_{\text{tgt}} = \frac{\pi D^2 A_{\text{tgt}} \tau_{\text{atm}} \tau_{\text{optics}} \text{PVF} \cdot \text{QE} \cdot \tau_{\text{int}}}{4R^2} \times [L_{\text{tgt}} - L_{\text{bg}}] \frac{\lambda_{\text{ave}}}{hc} \text{ electrons}. \quad (9a)$$

Integrating over wavelength for an integration time, the spectral differential target electrons is

$$\Delta n_{\text{tgt}} = \int_{\lambda} \frac{\pi D^2 A_{\text{tgt}} \tau_{\text{atm}}(\lambda) \tau_{\text{optics}}(\lambda) \text{PVF}(\lambda) \text{QE}(\lambda) \tau_{\text{int}}}{4R^2} \times [L_{\text{tgt}}(\lambda) - L_{\text{bg}}(\lambda)] \frac{\lambda}{hc} d\lambda \text{ electrons}. \quad (9b)$$

## 5. NOISE AND INTEGRATION TIME

All noise sources contribute to the SNR. Let  $n_{\text{BLIP}}$  be the number of photoelectrons produced by the sky background radiance,  $n_{\text{lens}}$  be the number of photoelectrons created by the lens emission, and  $n_{\text{dk}}$  be the detector dark current electrons. Assuming Poisson statistics, the variance is equal to the mean value. The variances add and the square root provides the rms value (root sum of the squares or RSS). The total rms noise in electrons is

$$N = \sqrt{n_{\text{BLIP}} + n_{\text{lens}} + n_{\text{dk}} + n_{\text{read}}^2} \text{ electrons rms}. \quad (10)$$

The readout noise  $n_{\text{read}}$  is usually expressed in rms electrons. Spatial fixed pattern noise FPN is usually specified as a fraction  $\alpha_{\text{FPN}}$  of temporal noise, so SNR is

$$\text{SNR} = \frac{\Delta n_{\text{tgt}}}{\sqrt{(1 + \alpha_{\text{FPN}}) n_{\text{BLIP}} + n_{\text{lens}} + n_{\text{dk}} + n_{\text{read}}^2}} \text{ unitless}. \quad (11)$$

Since there are ways to subtract out the FPN and target detection is performed by machine vision,  $\alpha_{\text{FPN}}$  is usually ignored.

For long-range detection, the sensor should be as close to BLIP limited as possible. Part of this design is to reduce the lens noise, dark current noise, and read noise. It is not always possible to eliminate the other noises, and the presence of these noise electrons can result in a shorter detector integration time or an increase in noise electrons.

Typical detectors today have an amplifier (either on-chip or off-chip) and a charge well (a capacitor associated with the

detector). For the older systems with an electronics bandwidth, the integration time can be estimated as the  $\tau_{\text{int}} = \frac{1}{2\Delta f}$ , where  $\Delta f$  is the electronics bandwidth in hertz (Hz). For modern detectors (both scanned and staring), there is a well capacity  $w_{\text{cap}}$  and an integration time  $\tau_{\text{int}}$  that affects the electrons collected. Even for digital readout integrated circuits (DROIC) that are finding their way into advanced IRST sensors (in both staring and scanned systems), there is an effective well capacity that includes a capacitor and a counter that can multiply the well capacity. For a standard MWIR staring sensor, a typical well capacity is anywhere from 5 to 10 million electrons. For a standard LWIR staring sensor, a typical well capacity is anywhere from 8 to 20 million electrons. DROIC systems can provide a well capacity exceeding 80 million electrons. DROIC systems do have additional electron noise associated with the transistors and switching. This additional noise can be added to the read noise. Typical read noise of standard infrared focal planes can be anywhere from 200 to 1000 electrons. Dark current for an InSb sensor can be on the order of  $5 \times 10^{-8}$  A/cm<sup>2</sup> and approximately  $5 \times 10^{-7}$  A/cm<sup>2</sup> for a MCT sensor. Dark current can vary dramatically for other detector materials.

There are two possible modes of operation. One way is to fix the integration time resulting in a variable well fill. The well must have sufficient capacity to avoid saturation. The more popular method provides a constant well fill, resulting in a variable integration time. The maximum time is limited by the frame time. Common well fill targets are 50% and 70%. If you allow a well fill to be too large (>70%), then the well can fill completely, and the background is saturated so there is no chance of detecting the target. The noise for the constant well fill assumption is

$$N = \sqrt{w_{\text{cap}}(\% \text{Fill}) + n_{\text{read}}^2} \text{ electrons rms.} \quad (12)$$

Since the read noise does not fill the capacitor, it is not part of the fill electrons. In this constant well fill assumption, the noise remains the same (how many electrons in the well fill). The signal is calculated using the integration time associated with Eq. (12), so SNR does vary with well capacity, percent well fill, and background flux.

Referring to Fig. 6, the background flux on a square detector (100% fill factor) is

$$P_p(\lambda, T) = L_p(\lambda, T) A_{\text{src}} \Omega = \frac{L_p(\lambda, T) d^2 \pi D^2}{4 f^2} \frac{\text{photons}}{\text{s}}. \quad (13)$$

The variable  $P_p(\lambda, T)$  is the power on the detector in photons per second, and  $f$  is the sensor focal length in meters. Equation (13) is the so-called camera formula where  $f/D$  is

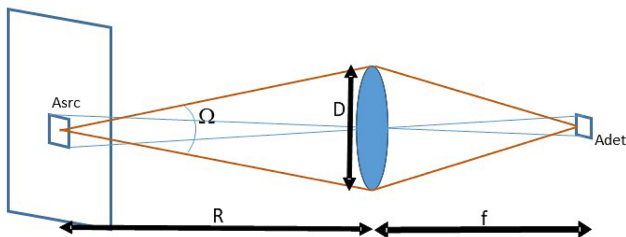


Fig. 6. Detector is receiving an IFOV worth of background radiance.

the optics  $f$ -number.  $L_p(\lambda, T)$  is the total atmospheric radiance in photons/s-cm<sup>2</sup>-sr. This quantity can be predicted by MODTRAN or estimated as an equivalent blackbody at sky temperature. If using MODTRAN or a sky measurement, it must be the entire sky radiance, which includes the background and path radiance as illustrated in Fig. 2. Notice that this flux measurement does not include the PVF since the background is a “resolved” measurement (the sky fills the detector). The number of photogenerated electrons per second produced by the background flux is

$$P_e(\lambda) = \frac{L_p(\lambda) d^2 \pi D^2 \tau_{\text{optics}}(\lambda) \text{QE}(\lambda)}{4 f^2} \frac{\text{electrons}}{\text{s}}. \quad (14)$$

The number of electrons generated during an integration time is

$$P_e = \frac{d^2 \pi D^2 \tau_{\text{int}}}{4 f^2} \int L_p(\lambda) \tau_{\text{optics}}(\lambda) \text{QE}(\lambda) d\lambda \text{ electrons.} \quad (15)$$

Setting  $P_e$  to the percent well fill and solving for the integration time provides

$$\tau_{\text{int}} = \frac{w_{\text{cap}}(\% \text{Fill}) 4 f^2}{d^2 \pi D^2 \int L_p(\lambda) \tau_{\text{optics}}(\lambda) \text{QE}(\lambda) d\lambda} \text{ s.} \quad (16)$$

This equation is valid if the system is BLIP limited and the lens and dark current contributions are minor. If the dark current and lens emission are significant, they too must be included in the well fill, thus reducing the integration time. Note that this action reduces the signal integration, but the resulting well fill noise remains the same. Finally, for the second case, where the integration time is not set to a certain well fill and it is set, Eq. (15) can be used to determine the BLIP noise electrons and the SNR can be calculated.

## 6. NOISE EQUIVALENT IRRADIANCE

The NEI [14–18] is a basic IRST parameter that guides sensor design, operation, and testing. As illustrated in Fig. 7, a small target whose irradiance  $E(\lambda)$  appears as power on a detector:

$$\Phi(\lambda) = E(\lambda) \tau_{\text{optics}}(\lambda) \frac{\pi D^2}{4} \text{PVF} \frac{\text{photons}}{\text{s-}\mu\text{m}}. \quad (17)$$

The resulting number of photoelectrons is

$$N = \frac{\pi \tau_{\text{int}} D^2 \text{PVF}}{4} \int_{\lambda_1}^{\lambda_2} E(\lambda) \tau_{\text{optics}}(\lambda) \text{QE}(\lambda) d\lambda \text{ electrons.} \quad (18)$$

If the irradiance is in W/μm, it must be converted to photons per second. If the system is BLIP limited, the

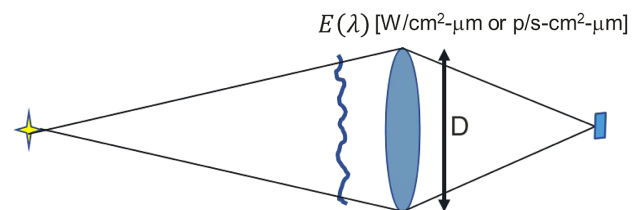


Fig. 7. Derivation of NEI.

noise is  $= \sqrt{w_{\text{cap}}(\% \text{fill})}$ . As appropriate, other noise components have to be added to  $N$ . The SNR is

$$\text{SNR} = \frac{\pi \tau_{\text{int}} D^2 \text{PVF}}{4\sqrt{w_{\text{cap}}(\% \text{fill})}} \int_{\lambda_1}^{\lambda_2} E(\lambda) \tau_{\text{optics}}(\lambda) \text{QE}(\lambda) d\lambda \quad \text{unitless.} \quad (19)$$

NEI is **defined** as the irradiance (differential) at the entrance aperture of a sensor that results in  $\text{SNR} = 1$ . Setting SNR to unity, assuming average values across the spectral region of interest, solving for the irradiance provides the broadband NEI

$$\text{NEI} = \frac{4\sqrt{w_{\text{cap}}(\% \text{fill})}}{\pi \tau_{\text{int}} \tau_{\text{optics}} \text{QE} D^2 \text{PVF}} \frac{\lambda_{\text{ave}}}{hc} \frac{\text{photons}}{\text{s-cm}^2}. \quad (20)$$

Using everything that we have learned in the SNR derivation for a BLIP-limited sensor,

$$\text{SNR} = \int_{\lambda_1}^{\lambda_2} \frac{I(\lambda) \tau_{\text{atm}}(\lambda)}{R^2} \frac{\tau_{\text{optics}}(\lambda) \text{QE}(\lambda) \pi D^2 \text{PVF} \tau_{\text{int}}}{4\sqrt{w_{\text{cap}}(\% \text{fill})}} d\lambda \quad \text{unitless.} \quad (21)$$

The first term inside the integral is the irradiance (intensity divided by range squared), and the second term is  $1/\text{NEI}$  of the sensor. From this expression, we can provide a spectral NEI

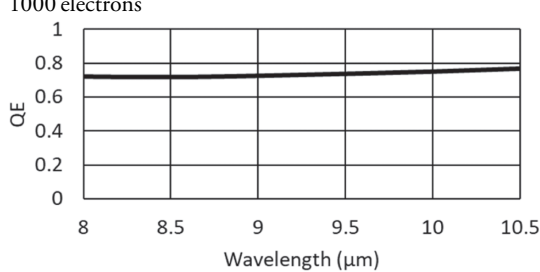
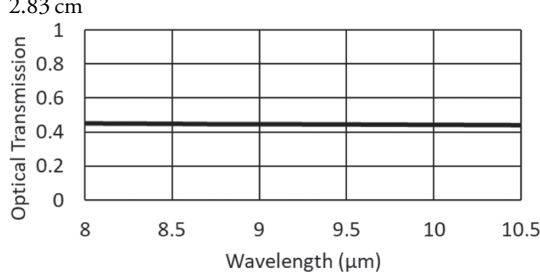
$$\text{NEIS}(\lambda) = \frac{4\sqrt{w_{\text{cap}}(\% \text{fill})}}{\tau_{\text{optics}}(\lambda) \text{QE}(\lambda) \pi D^2 \text{PVF} \tau_{\text{int}}} \frac{\text{photons}}{\text{cm}^2}. \quad (22)$$

As an example, consider a LWIR staring sensor with the characteristics listed in Table 1.

The maximum integration time provided in Table 1 would overflow the well capacity. Since 65% is specified as well fill (and it is calculated on the photon background flux), we end up with 7.8 million electrons generated by background flux, which provides an integration time of 0.147 ms. The dark current is  $6.1 \times 10^{-7} \text{ A/cm}^2$  times a detector area of  $2.25 \times 10^{-6} \text{ cm}^2$ , yielding  $1.37 \times 10^{-12}$  amps or coulombs per second. With an electron at  $1.6 \times 10^{-19} \text{ C}$ , the dark current is  $8.6 \times 10^6$  electrons per second. With an integration time of 0.147 ms, the dark current generates 1260 electrons in the well, which is negligible compared to the background flux noise. Read noise is also negligible at 1000 electrons.

The NEI calculations are provided in Fig. 8 for both broadband and spectral quantities. With the  $F/1.8$  optics, the integration time required increases, but this does not fully account for the loss in both signal and noise. The PVF reduces the signal because the optical blur spills more onto adjacent detectors. The  $F\lambda/d_{\text{cc}}$  value is 0.905, resulting in

**Table 1. Representative LWIR Sensor**

Parameter	Value
Material	Mercury Cadmium Telluride (MCT)
Detector pitch	15 $\mu\text{m}$
Fill factor	100%
Format	4000 by 4000 (detectors)
Field of view	70° by 70°
Band	8.0–10.1 $\mu\text{m}$
Well capacity	12 million electrons
Dark current	$6.1 \times 10^{-7} \text{ A/cm}^2$
Read noise	1000 electrons
Quantum efficiency	
Frame rate	60 Hz
Focal length	4.25 cm ( $F = 1.5$ ) 5.09 cm ( $F = 1.8$ )
Aperture diameter	2.83 cm
Optical transmission	
Integration time	1.7 ms max or 65% of well capacity

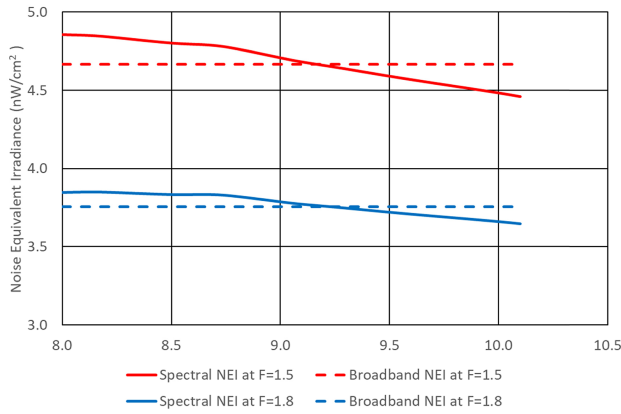


**Fig. 8.** Noise equivalent irradiance in  $W/cm^2$  and  $pW/cm^2\text{-}\mu m$ .

an average PVF of 0.467. The broadband NEIs are 0.467 and  $0.376 pW/cm^2$ , respectively.

## 7. TARGETS

Airborne target signatures are typically specified by an intensity in  $W/sr$  or  $W/sr\text{-}\mu m$ . Depending on the analysis approach, these quantities may require conversion to photons/ $s\text{-}sr$  or photons/ $s\text{-}sr\text{-}\mu m$ . NEI is frequently provided in  $W/cm^2$ , so measurements of aircraft signatures are typically provided in  $W$ . However, if an advancedIRST system is under consideration with staring focal plane, deep electronic wells, or digital ROICs, then the target radiometry must be converted to photons per second.

### A. Graybody Target

Airborne targets are sometimes considered blackbodies, where the spectral radiant existence is

$$M_e(\lambda, T) = \epsilon(\lambda) \frac{c_1}{\lambda^5} \frac{1}{\left[\exp\left(\frac{c_2}{\lambda T}\right) - 1\right]} \frac{W}{m^2\text{-}\mu m} \quad (23a)$$

or

$$M_q(\lambda, T) = \epsilon(\lambda) \frac{c_3}{\lambda^4} \frac{1}{\left[\exp\left(\frac{c_2}{\lambda T}\right) - 1\right]} \frac{\text{photons}}{s\text{-}m^2\text{-}\mu m}. \quad (23b)$$

The constants are  $c_1 = 3.74 \times 10^8 W\text{-}\mu m^4/m^2$ ,  $c_2 = 14388 \mu m\text{-}K$ , and  $c_3 = 1.884 \times 10^{27} \text{photons}\text{-}\mu m/s\text{-}m^2$ . The variable  $\epsilon$  is the target emissivity, and  $T$  is the target absolute temperature. For a target that is the front of a missile dome [half a hemisphere with dome radius  $r$  in centimeters (cm)] as seen by the sensor, it does not matter if the target is treated like a spherical emitter or a Lambertian emitter with a flat surface. For a spherical emitter, the surface of the hemisphere is  $2\pi r^2$  and the flux emission is in  $2\pi$  steradians, and for a Lambertian emitter, the surface is  $\pi r^2$  and the emission is in  $\pi$  steradians. From Eq. (23), the target intensity is

$$\begin{aligned} I_e(\lambda T) &= M_e(\lambda, T) \frac{A_{\text{tgt}}}{\pi} \\ &= \epsilon(\lambda) \frac{A_{\text{tgt}}}{10^4} \frac{c_1}{\pi \lambda^5} \frac{1}{\left[\exp\left(\frac{c_2}{\lambda T}\right) - 1\right]} \frac{W}{sr\text{-}\mu m} \end{aligned} \quad (24a)$$

or

$$\begin{aligned} I_q(\lambda T) &= M_q(\lambda, T) \frac{A_{\text{tgt}}}{\pi} \\ &= \epsilon(\lambda) \frac{A_{\text{tgt}}}{10^4} \frac{c_3}{\pi \lambda^4} \frac{1}{\left[\exp\left(\frac{c_2}{\lambda T}\right) - 1\right]} \frac{\text{photons}}{s\text{-}sr\text{-}\mu m}. \end{aligned} \quad (24b)$$

Note that Planck's blackbody expression is usually specified in meters. The factor  $10^4$  converts target area from  $cm^2$  to square meters ( $m^2$ ). We use the area of the target as  $\pi r^2$ . Graybody targets as provided by intensities of Eq. (24) are frequently used for cold hardbody missiles (where the dome is pointed at the sensor) as well as aircraft hardbody (without exhaust) and some drones. Equation (24) can be used in a spectral form, or it can be integrated to provide a broadband quantity. For a 320 K graybody missile with emissivity over the 8–12  $\mu m$  band of 0.98, the total emittance is  $0.016 W/cm^2$ , and its radiance is  $0.0051 W/cm^2\text{-}sr$ . If it has a nose radius of 0.25 m, the broadband target intensity is  $10.0 W/sr$ . In photons per second, the emittance is  $8.11 \times 10^{17} p/s\text{-}cm^2$  and the radiance is  $2.58 \times 10^{17} p/s\text{-}cm^2\text{-}sr$ . The target radiance and target area provide an intensity of  $5.07 \times 10^{20} p/s\text{-}sr$ . The graybody target can be used spectrally with the equations above and will provide a more accurateIRST calculation for SNR.

### B. Differential Radiance or Intensity

From Eqs. (1)–(8), it can quickly be determined that target intensity or radiance is not the primary driver behind SNR. It is the *difference* between the target intensity (or radiance) and the background equivalent intensity or radiance. Since the background provides a radiometric pedestal that the target is seen against, the difference between the target and background are critical in the SNR calculation. While a target intensity already includes the target dimensions as part of the emission, the target size must be known to determine how much background is subtracted from the target intensity to get the differential target intensity (or radiance). This difference can be converted to a target to background intensity by multiplying the radiance by the target size in  $cm^2$ . So the target area is a fundamental parameter that must be used to determine the background intensity so that the difference in target and background radiance or intensity can be determined. The background intensity is determined by multiplying the target area (at the target range) times the background radiance in Fig. 2.

### C. High-Speed Targets

For high-speed targets (Mach numbers above 0.3), the target temperature is a function of the ambient flight temperatures and the Mach number [19]. An approximation is

$$T_{\text{tgt}} = b T_{\text{ambient}} \left( 1 + r \frac{(\gamma - 1)}{2} \text{Mach}^2 \right) K, \quad (25)$$

where  $r$  is the recovery parameter (0.84 for laminar and 0.89 for turbulent),  $\gamma$  is the adiabatic index (around 1.4 for air), and  $b$  is a constant that reflects gas effects. For Mach numbers below 6,  $b$  is around 1, and for Mach numbers above 8,  $b$  is 0.5. This  $T_{\text{tgt}}$  is then used in Planck's equation.



## D. Broadband Intensity Models/Measurements

There are sophisticated aircraft target models that predict both broadband and spectral target intensities. There are also measurement activities that measure the intensity signatures of aircraft and can provide broadband intensity in W/sr as a function of azimuth and elevation angles. Figure 9 shows a notional aircraft broadband LWIR intensity plot as a function of azimuth and elevation angle. Azimuth angle is shown on the polar plot from 0° to 360° around the aircraft and refers to the yaw or heading angle of the aircraft, where 0° is the IRST sensor looking at the aircraft head on. Elevation angle refers to the pitch angle of the aircraft relative to the observer/sensor, where 0° elevation means the aircraft is level with the observer/sensor.

In addition to broadband intensity, spectral intensity for a given target azimuth and elevation angle can be provided. Figure 10 shows a notional spectral target intensity as a function of W/sr- $\mu\text{m}$ . Such an intensity peaking in the LWIR band corresponds to a hardbody aircraft or missile target, where the skin temperature of the target is not much higher than the ambient background. Targets with exhaust and rocket motors have much more spectral variation and provide spectral content at much shorter wavelengths.

There are a large number of sources (both open to the public and private) that provide estimates for aircraft intensity signatures. The signatures can be modeled, simulated, or measured, and using these target signatures in small target detection estimates is an important part of target signature acquisition. Reference [20] provides a model that predicts different components of aircraft intensity signatures to include engine, fuselage, wings, and so on, and it does so in a spectral intensity format. It allows the aircraft designers as well as the sensor developers to consider all of the aircraft components and what their contributions are to the overall signatures. Models, simulations, and measurements can provide different levels of fidelity to include spatial, spectral, and temporal characteristics. Figure 9 only shows integrated broadband intensity that is not a function of target spatial characteristics (i.e., spectral is integrated and spatial is integrated). Figure 10 only shows a spatially integrated intensity spectrum for a single sensor look angle. It is rare where aircraft measurements include good fidelity across all measurement parameters such as spatial, spectral, and temporal. In

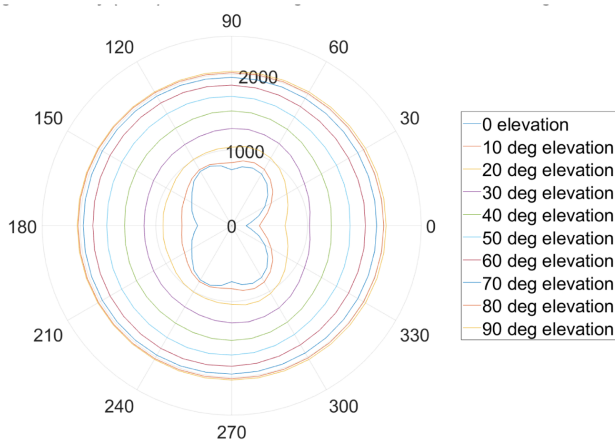


**Fig. 9.** Broadband target intensity in W/sr as a function of azimuth angle and elevation angle.

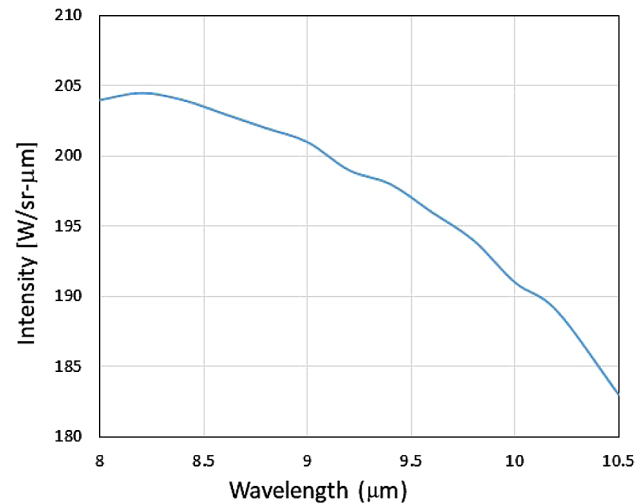


**Fig. 10.** Notional target spectral intensity.

other sensing applications such as threat warning (e.g., Infrared Countermeasures [IRCM]), temporal target profiles can be critical in the discrimination of potential small targets.

As drones proliferate and the detection of drones becomes a more important sensor function, the signatures of drones are needed. Reference [21] provides some preliminary infrared drone signatures that can be used for IRST sensor estimates. In this case, both MWIR and LWIR signatures are measured spatially, but they are integrated over the two primary infrared emission bands. The measurements were taken during the daytime and include solar effects. Spectral measurements as well as temporal measurements are not included as instruments that can measure these characteristics simultaneously are extremely expensive and are usually developed as custom sensors.

## 8. ATMOSPHERIC BACKGROUND AND PATH RADIANCE

In Fig. 2, the atmosphere emits radiance from both the background (behind the aircraft) and the path between the target and the sensor. The total atmospheric radiance seen in the sky by the sensor is

$$L_{\text{total}} = L_{\text{bg}} + L_{\text{path}} \frac{\text{W}}{\text{cm}^2\text{-sr}} \quad \text{or} \quad \frac{\text{photons}}{\text{s}\text{-cm}^2\text{-sr}} \quad (26a)$$

and spectrally

$$L_{\text{total}}(\lambda) = L_{\text{bg}}(\lambda) + L_{\text{path}}(\lambda) \frac{\text{W}}{\text{cm}^2\text{-sr}\text{-}\mu\text{m}} \quad \text{or} \quad \frac{\text{photons}}{\text{s}\text{-cm}^2\text{-sr}\text{-}\mu\text{m}}. \quad (26b)$$

There are two ways to calculate the power on the detector from a differential target intensity. One is from Eq. (4), where the path radiance from the target and the background radiance cancels out in the difference. The other is with path radiance, where Eq. (4) is modified to include the total sky radiance. The broadband differential target power is

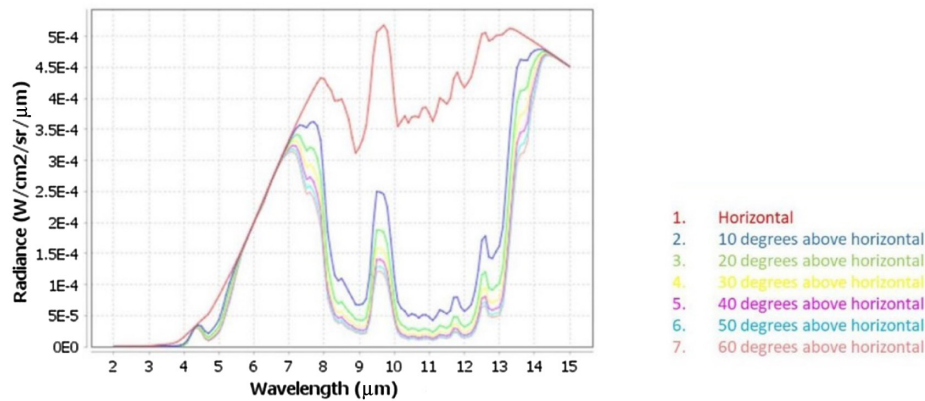


**Fig. 11.** MODTRAN US standard sky radiance as a function of elevation angle.

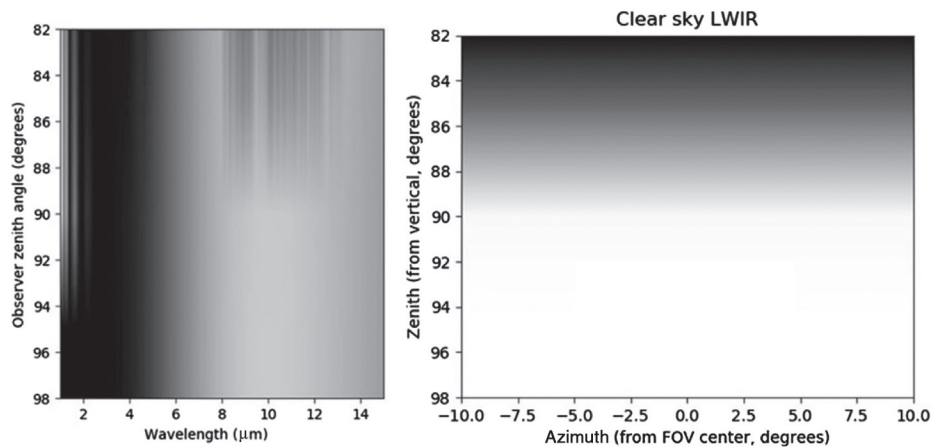


**Fig. 12.** MODTRAN sky radiance and integrated LWIR sky radiance.

$$\Delta P_{\text{tgt}} = \frac{\pi D^2 A_{\text{tgt}} \tau_{\text{atm}}}{4R^2} [(L_{\text{tgt}} + L_{\text{path}}) - (L_{\text{total}})] W, \quad (27a)$$

and the spectral differential target power is

$$\Delta P_{\text{tgt}}(\lambda) = \frac{\pi D^2 A_{\text{tgt}} \tau_{\text{atm}}(\lambda)}{4R^2} \times [(L_{\text{tgt}}(\lambda) + L_{\text{path}}(\lambda)) - L_{\text{total}}(\lambda)] \frac{W}{\mu\text{m}}. \quad (27b)$$

For the broadband differential target electrons, Eq. (8) becomes

$$\Delta n_{\text{tgt}} = \frac{\pi D^2 A_{\text{tgt}} \tau_{\text{optics}} \text{PVF} \cdot \text{QE} \cdot \tau_{\text{int}}}{4R^2} \times [L_{\text{tgt}} \tau_{\text{atm}} + L_{\text{path}} - L_{\text{total}}] \frac{\lambda_{\text{ave}}}{hc} \text{ electrons}, \quad (28a)$$

and the spectral differential is

$$\Delta n_{\text{tgt}}(\lambda) = \int_{\lambda} \frac{\pi D^2 A_{\text{tgt}} \tau_{\text{optics}}(\lambda) \text{PVF}(\lambda) \text{QE}(\lambda) \tau_{\text{int}}}{4R^2} \times [L_{\text{tgt}}(\lambda) \tau_{\text{atm}}(\lambda) + L_{\text{path}}(\lambda) - L_{\text{total}}(\lambda)] \frac{\lambda}{hc} \text{ electrons}. \quad (28b)$$

In all atmospheric radiance quantities, the geometry of the measurement or atmospheric model is extremely important as well as the climate, temperature, and humidity of the air. Figure 11 shows MODTRAN calculations for sky radiance as a function of elevation angle. The horizontal view is the sky radiance just above the horizon, and the other angles are 10° in sensor elevation look angle. The path radiance decreases with elevation angle as shown. In this case, we extend the wavelength range so that the reader can see the radiance across multiple bands of interest.

Figure 12 shows a different rendition of Fig. 11, where the path radiance is presented in a gray level as a function of elevation angle and spectrum. The figure on the right is the integrated LWIR sky radiance from 8 to 12 μm. The path radiance below the horizon is just a 300 K blackbody and corresponds to the ground. As the sky radiance increases, the gray scale transitions from black to white. Note that as the path radiance decreases, the atmospheric transmission increases.

MODTRAN can provide very good results provided that the atmospheric parameters are chosen correctly. Figure 13 shows some sky path radiance measurements in the LWIR (8–14 μm) in Memphis, Tennessee, in the summer of 2017, where MODTRAN atmospheres are compared in terms of a mid-latitude summer, a tropical, and a corrected mid-latitude summer. The corrected atmosphere used both the

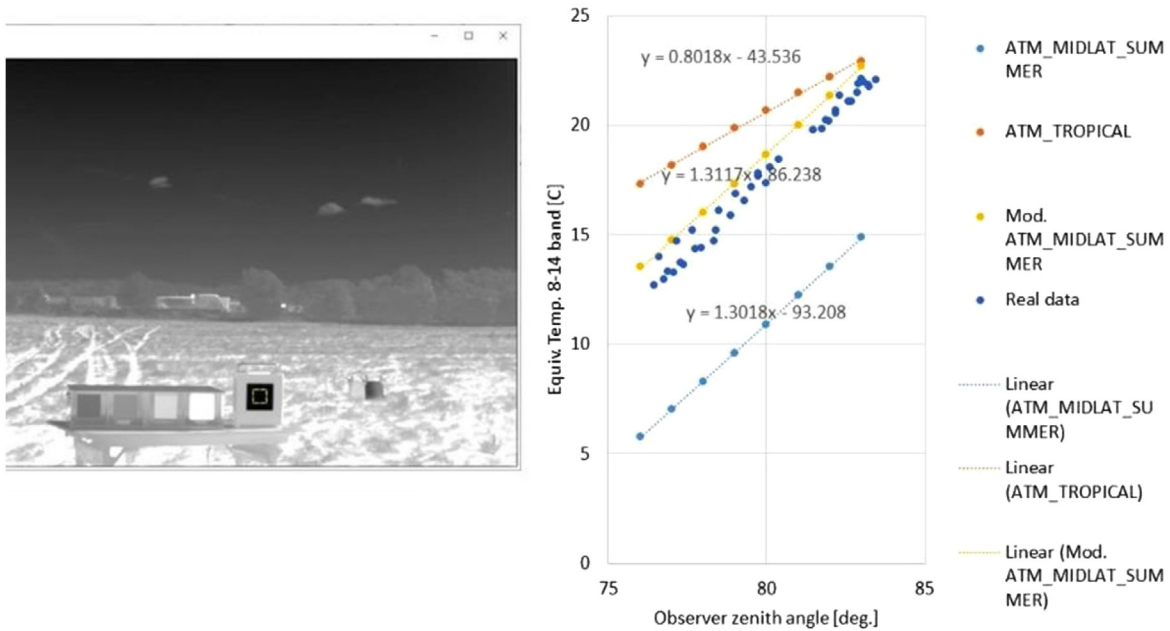


Fig. 13. Memphis sky measurements versus MODTRAN estimates for sky radiance.

Table 2. Broadband SNR Example<sup>a</sup>

Range (km)	BG Radiance (mW/cm <sup>2</sup> -sr)	Tgt Radiance (mW/cm <sup>2</sup> -sr)	Diff. Radiance (mW/cm <sup>2</sup> -sr)	Transmission (unitless)	Diff. Irradiance (pW/cm <sup>2</sup> )	NEI (pW/cm <sup>2</sup> )	SNR (unitless)
10	0.113	4.40	4.287	0.895	271.0	0.467	580.2
20	0.097	4.40	4.303	0.840	63.9	0.467	136.7
30	0.086	4.40	4.314	0.801	27.1	0.467	58.1
40	0.077	4.40	4.323	0.771	14.7	0.467	31.5
50	0.070	4.40	4.330	0.746	9.1	0.467	19.5
60	0.064	4.40	4.336	0.725	6.2	0.467	13.2
70	0.060	4.40	4.340	0.707	4.4	0.467	9.5
80	0.056	4.40	4.344	0.691	3.3	0.467	7.1
90	0.052	4.40	4.348	0.677	2.6	0.467	5.5
100	0.049	4.40	4.351	0.665	2.0	0.467	4.4

<sup>a</sup>F = 1.5.

measured temperature and humidity, and it was corrected in the MODTRAN inputs. Note that the equivalent temperature of the sky path varies dramatically, but the modified atmosphere closely matches the sky measurements with the LWIR radiometer. Also, note that the different atmospheres can vary the path radiance by 10 K, where typicalIRST differential temperatures can be as low as a few Kelvin or less. Significant errors are manifested by incorrect atmospheric path radiance.

### 9. BROADBAND EXAMPLE

As a broadband example, we provide a challenging case where the sensor used in the NEI example (Table 1, F = 1.5 data) is applied to a commercial head-on aircraft with no view of the engine exhaust. For the target, we use an effective target diameter of 3 m with a target area of 7.1 m<sup>2</sup>. With a “cold” front view of the aircraft, we assume the aircraft has an equivalent blackbody radiance of 350 K, providing an average target radiance of 4.4 × 10<sup>-3</sup> W/cm<sup>2</sup>-sr in the band of 8.0–10.1 μm. The altitude of both the sensor and the target aircraft were 10 km,

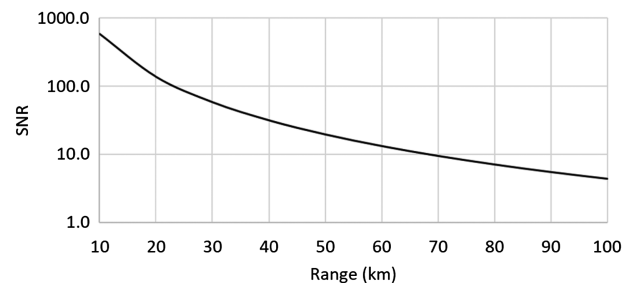


Fig. 14. Broadband SNR example.

and the atmosphere we used was the US Standard MODTRAN atmosphere. We used MODTRAN to calculate the background radiance for each of the ranges as well as the atmospheric transmission between the target and the sensor for each of the ranges. The *average* background radiance and transmission from MODTRAN for each range is provided in Table 2.

Detection of a relatively cool target (350 K) requires a sensitive sensor similar that is detailed in Table 1 with the

$F/1.5$  case shown in Fig. 8. The broadband NEI is taken to be  $0.467 \text{ pW/cm}^2$ . Finally, the SNR is provided as the ratio of the two. Figure 14 shows the SNR as a function of range. Typically, sensor designers assume  $\text{SNR} = 10$  is required for high probability target detection. Some designers use  $\text{SNR} = 6$ . Therefore, this aircraft should be detected somewhere between 70 and 80 km.

### 10. SPECTRAL EXAMPLE

We now perform the same example with spectral quantities. Equation (5b) is used to determine the spectral irradiance on the entrance aperture of the sensor. Figure 15 illustrates the MODTRAN predicted sky radiance (behind the target). The atmospheric transmission is illustrated in Fig. 16. It is a function of wavelength and range to the target. As in the broadband example, we assume a blackbody equivalent target with 350 K and a band of 8–10.1  $\mu\text{m}$ . Using the blackbody radiance, the background radiance, and the atmospheric transmission, Eq. (5b) provides the spectral irradiance (target to background differential) in Fig. 17. The spectral differential target irradiance is divided by the spectral NEI to provide SNR as a function of wavelength. The resulting integrated SNR is provided in Fig. 18.

At 70 km, the broadband SNR is 9.5 compared to the spectral SNR, which is 9.6. The mathematical complex spectral approach is always more accurate than the broadband calculation. Errors are even more significant for MWIR calculations (the edge of Planck’s curve) as well as for targets, atmospheres, and sensors that vary significantly over the spectral region of interest.

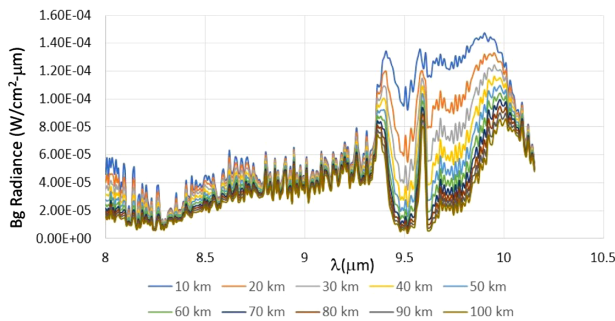


Fig. 15. Background spectral radiance predicted by MODTRAN.

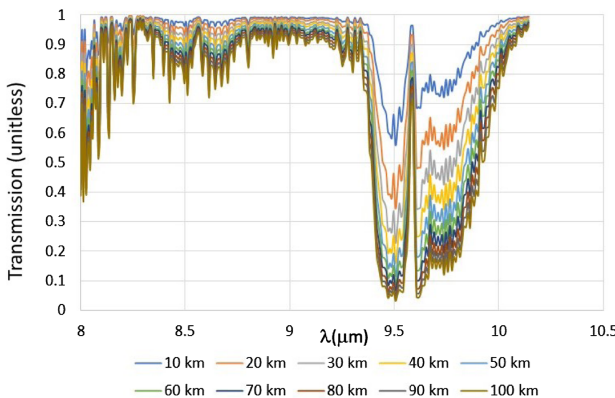


Fig. 16. Atmospheric spectral transmission as a function of range.

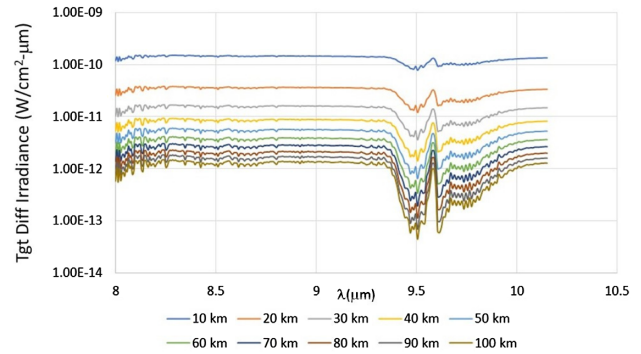


Fig. 17. Spectral differential target irradiance on the sensor aperture.

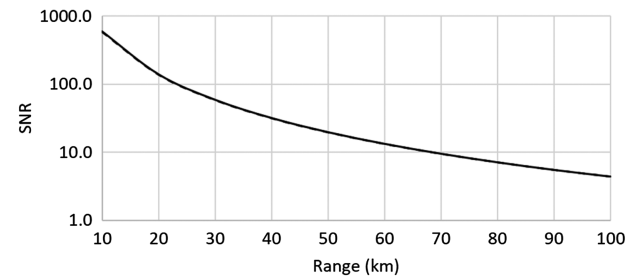


Fig. 18. Spectral calculation resulting in SNR as a function of range. Spectral is the solid line, and broadband is the dashed line. For this example, the difference ranges from 2.3% to 0.8%.

### 11. OPTIMIZATION OF SYSTEM PERFORMANCE

Section 4 discussed PVF in detail. This section predicts the SNR as a function of  $F\lambda/d_{cc}$  and PVF. Figure 19 illustrates three different  $F\lambda/d_{cc}$  cases.

Figure 20 illustrates the general performance trends for MWIR and LWIRIRST systems. As we previously defined the PVF best case (ensquared energy), worst case (corners), and average case (average of random locations), the optimized SNR for each case is a function of  $F\lambda/d$ . The best, worst, and average case optimizations are  $F\lambda/d$  of 0.84, 1.1, and 1.75, respectively. These optimizations assume an infinite well capacity with a 16 ms detector integration time. To demonstrate this concept, a background-limited IIRST in the LWIR was modeled with SNR calculated resulting in the middle graph corresponding to

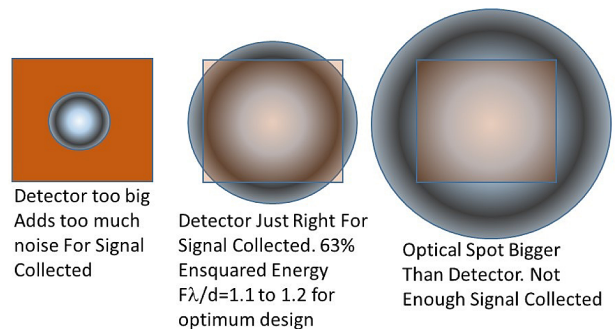
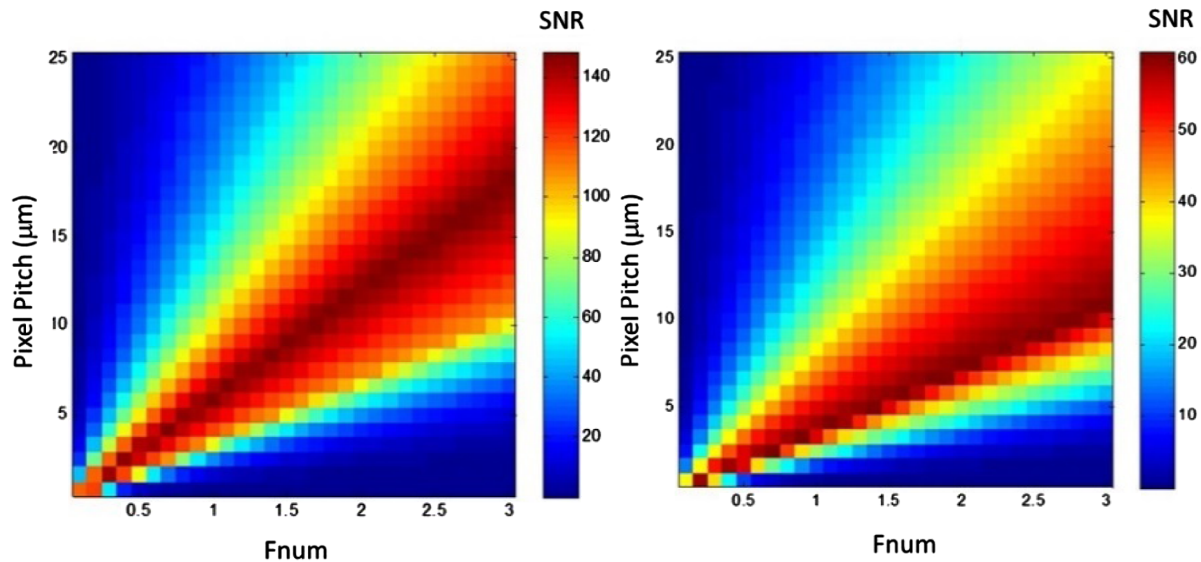
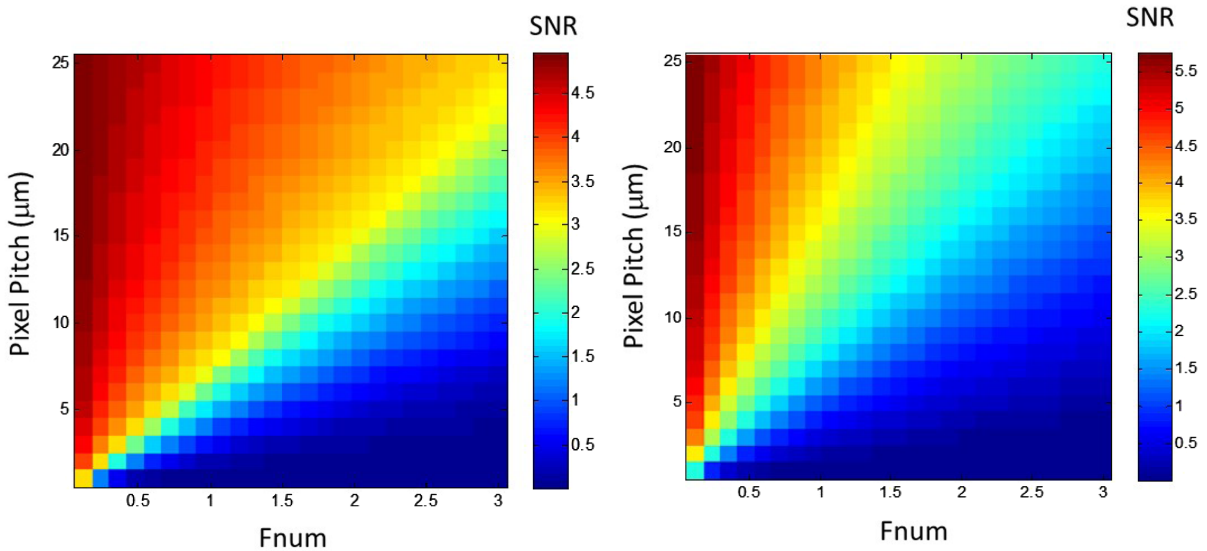


Fig. 19. Optical spot size compared to detector size. Left to right  $F\lambda/d_{cc} \sim 0.1, \sim 0.4, \text{ and } \sim 0.57$ .



**Fig. 20.** LWIR SNR for charge well of 100 Me<sup>-</sup> (left) and 12 Me<sup>-</sup> (right). Note the different SNR scales.



**Fig. 21.** Constant format benefit of larger detectors. SNR for MWIR on left and SNR for LWIR on the right.

a 100 Me<sup>-</sup> well capacity. The graph to the right corresponds to a 12 Me<sup>-</sup> well capacity.

Other parameters can modify the SNR performance, such as dark current and read noise. References [12,22] provide a complete description of how detector parameters can change the optimization of the IRST function. The equations in this paper provide for the means to change detector well capacity and integration time.

A final assumption associated with the optimization guidance of Fig. 20 is that the detector chip is of limited size and the detectors can be any size. A larger chip provides much higher performance, because a larger chip for the same FOV provides a longer focal length and larger aperture size. From the SNR equation, aperture diameter is the most important parameter in IRST performance since it is squared dependency and all others are linear or root functions. So an artefact of the aperture

importance is the design associated with constant chip size. For example, if it is known that a 4 K by 4 K format focal plane will be used but detector size is flexible, then larger detectors provide for more SNR. Figure 21 illustrates MWIR to the left and LWIR to the right for a 70° IRST with 16 ms integration time and 75% well fill. The aperture and focal length were varied (constant  $F = 1.5$ ) to accommodate various detector sizes (pixel pitch). As it can be observed, the larger detectors provide more SNR primarily because the corresponding chip size is bigger, meaning the focal length and aperture diameter are larger.

## 12. SCANNED VERSUS STARING SYSTEMS

While the previous section attempted to find an optimization for staring arrays, there are other configurations that are worth considering. In one study [23], the architectures of staring

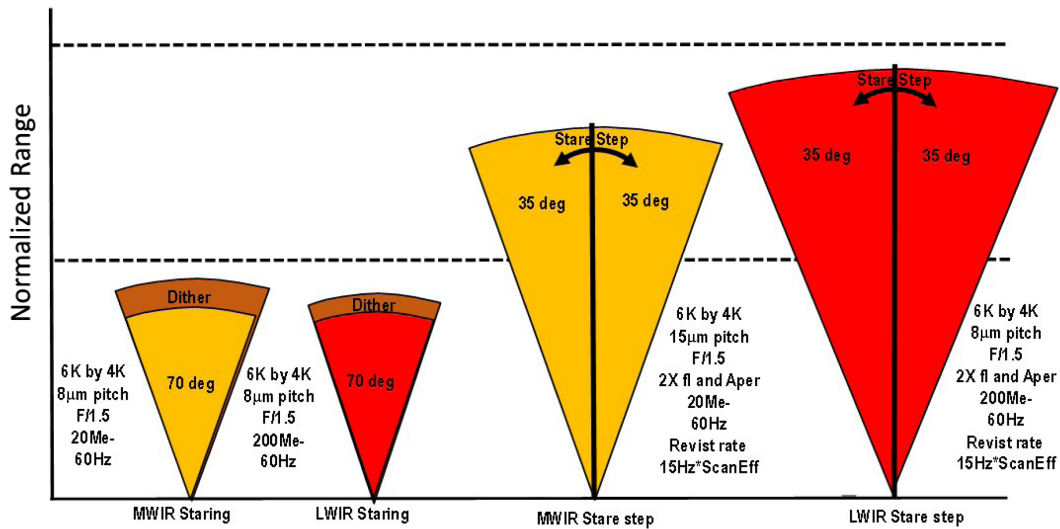


**Fig. 22.** Comparison of staring, dither, and stare step.

versus dither versus stare step were compared. That is, the second, third, and fourth architectures in Fig. 3 were compared with the same physical focal plane. In this study, the field-of-regard collection was time constrained, and duty cycle (either deep wells or high frame rates) was enabled, with stare step and dither being used as mechanisms for trading space with time. The cases compared were basic staring (with and without deep wells), dithered, and stare-step systems.

In Fig. 22, a comparison calculation provides range performance for a sensor that is a 6 K by 4 K MWIR and LWIR format with a 70° FOV. The sensor had an 8 µm pitch detector (both MWIR and LWIR). Both sensors had an  $F/1.5$  optic with a 60 Hz frame rate. The well capacity of the MWIR and LWIR sensors were 20 Me<sup>-</sup> and 200 Me<sup>-</sup>, respectively (note that the LWIR photon flux is roughly 10 times that of MWIR). The yellow cone shows the MWIR coverage range, and the red shows the LWIR coverage range, where the staring performance is shown by the two fans on the left side of the graph. The brown fan extension shown on the MWIR and LWIR sensor is due to a 4 pt dither function, where the frame rate is reduced to 15 Hz, but the resolution is increased with the dither function. Note that resolution is not increased due to a doubling of the sampling frequency, but the aperture size remains the same, so a dramatic increase in sensitivity and resolution is not realized. On the right side of the graph, the same focal plane is configured with an increase in both focal length and aperture by a factor of 2, thus reducing the FOV to 35°. The sensors are stare stepped, meaning a gimbal or fast mirror moves the FOV left and right to provide a combined FOV of 70° (we call this field of regard or FOR). Note that for both cases, the range increases significantly with an increase in resolution and sensitivity (larger aperture).

From Fig. 22, staring and dithered IRST systems cannot compete with stare-step and scanned systems (the scanned system is the left architecture in Fig. 3) due to the smaller apertures. In the comparison of scanned versus stare-step IRST systems, consider Fig. 23. We again consider a 6 K by 4 K focal plane in both the MWIR (3–5 µm) and LWIR (8.0–10.1 µm) and an FOR of 90° against a cool target. A pitch of 8 µm is assumed as

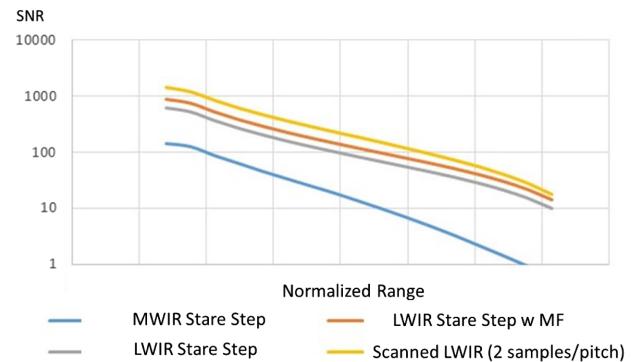


**Fig. 23.** Stare-step MWIR, stare-step LWIR, stare-step LWIR with matched filter, and scanned TDI LWIR.

well as a quantum efficiency of 70%. We allow a well capacity of 80 Me<sup>-</sup> in the MWIR and 400 Me<sup>-</sup> in the LWIR with dark current and read noise commensurate with MCT and InSb focal planes, respectively. We design a FOV of 7.9 by 5.25 with a focal length of 35 cm and an aperture of 23.3 cm. The instantaneous FOV for both cases is 22.9 microradians. The  $F\lambda/d$  for the MWIR is 0.75 and the LWIR is 1.7. For the stare-step MWIR and LWIR cases, there are 12 FOVs across the FOR. The FOR revisit rate is 2 s, so with some mirror settle time and scan efficiency, the integration time of the stare-step sensors is 38 ms. With the stare-step sensors, there are 68,722 detector samples across the FOR. The LWIR scanned TDI sensor (using the same 6 K by 4 K LWIR focal plane), there are two samples per instantaneous FOV, so there are 137,444 samples across the FOR. The LWIR scanned system has corresponding detector integration time of 0.006 ms, but the scanned system has a TDI factor of 6000 detectors in the scan line.

Figure 23 shows the comparison of the MWIR stare step, the LWIR stare step, a LWIR stare step with a matched filter (MF), and the scanned LWIR system. The MF integrates the SNR over some number of detectors since the  $F\lambda/d$  over 1.1 has a blur spot that spills over on adjacent detectors. The MWIR stare step does not perform as well as the LWIR stare step. The

LWIR performance (SNR) provides a longer range performance in the stare-step configuration. Using the matched filter, the LWIR stare step provides a marginal increase in SNR as a function of range. Finally, the scanned LWIR TDI sensor provides the highest performance. The primary reason for the higher performance scanned system is that there are two samples per detector footprint, giving a higher PVF over the FOV of the system. This is the only difference, since all other aspects of the stare step and scanned system are identical.

In general, we can say that staring and dither IRST systems are limited in performance mainly due to aperture size. Stare-step and scanned TDI IRST systems are comparable in performance, but MWIR and LWIR trades are worthwhile depending on desired targets. However, the complexity of stare-step and scanned systems include mechanical scanning considerations as well as ROIC trades.

### 13. DISCUSSION

There are a number of important lessons that can be gleaned from the small target detection trades that have been conducted over the years. There is definitely a high interest in using staring focal planes in IRST systems above line scanners and TDI implementation of smaller format focal planes. The interest in large format arrays allows for use of these arrays in a scanned TDI approach as well as a stare-step approach for high performance. There are distributed aperture systems that use a static single focal plane for small target detection over large angles, but the performance of these systems is limited.

In the execution of trade studies [24], the following observations are worthwhile to consider in small target detection:

- Instantaneous field of view (IFOV) is not a good primary metric to describe IRST sensor performance. It may have been a good metric in the past due to single detector size options, but with the variety of detector sizes now, dramatic differences in performance can be seen with the same IFOV (e.g., a small detector with a small aperture versus a large detector with a larger aperture).
- The primary IRST parameter associated with performance is optical aperture diameter. There is a squared law dependence on SNR. All other parameters are not as strong in influencing performance.
- The second most important parameter is focal plane chip size. Bigger is better. A larger chip size allows for a larger FOV or allows for a longer focal length which, in turn, provides for a larger aperture.
- It is extremely difficult to design a staring array system with wide FOV and good long-range performance without a stare-step or scanning action. A stare step and scanning allows a narrower FOV that results in a longer focal length and, thus, a larger aperture diameter.
- Contrary to intuition, many small detectors do not help performance significantly.
- Deep wells or fast framing (both of these correspond to larger duty cycle collecting photons) can increase performance significantly.
- Dither helps performance (for low  $F\lambda/d$ ) but not nearly as much as stare step.

- A MF helps for systems with high  $F\lambda/d$ . After detector size increases so that  $F\lambda/d$  goes below 1.1, then a MF does not enhance range performance significantly.

All these lessons are worthwhile in the design of IRST systems. On the issue of MWIR versus LWIR, it really depends on the target and the atmospheric conditions. In many cases, LWIR performs better than MWIR.

One issue that was not addressed in this paper is that of performance in clutter (most IRST systems are clutter limited, but you need a decent SNR as a minimum, so this paper is helpful). IRST performance in clutter conditions is an extremely important consideration. It is common for clutter to dominate over temporal noise by more than an order of magnitude when the sensor is looking for a point source target against typical scene clutter; terrestrial, clouds, ocean, and so on. A matched filter is used to maximize SNR for a point source against a uniform background with white temporal noise. Scene clutter is not white, but rather follows a Wiener power spectrum. Therefore, a combination of MF (low pass) and high-pass filter combine to create a bandpass filter, wherein the matched filter suppresses the high-frequency temporal noise and the high-pass filter rejects the low-frequency clutter. Thus, the combination maximizes the signal to clutter and noise ratio. The high-pass filter is roughly (1-MTF), where MTF includes the optics and detector. Historically, it is common to use the only the detector SINC function for the MTF. This used to be a reasonable approximation because the detector was large relative to the Airy disk (low  $F\lambda/d$ ), so IFOV dominated the MTF. As detector size and pitch decrease, the diffraction MTF becomes the dominant MTF. In summary, large aperture diameter is again an important factor to achieve high IRST performance.

### 14. CONCLUSIONS

Small target detection and IRST systems are complicated and sometimes difficult to understand. We have provided a tutorial for those interested in working the small target detection problem to include the IRST function. The tutorial includes terms and nomenclature as well as the equations necessary to calculate broadband and spectral SNR as a function of range. The spectral calculations can be performed using watts or photons per second and yield the same results. We have also provided some guidance on the optimization of small, unresolved, target detection sensor optimization. The optimization and the trades include MWIR versus LWIR as well as scanned, dithered, stare-step, and scanning comparisons. We provide some general guidance that should not replace your own trades for specific targets, atmospheres, and sensors. Finally, while clutter dominates the performance of most systems, we only provide the SNR calculations in this tutorial because it is the first step in a successful small target detection sensor. There are hundreds, if not thousands, of papers on the subject of signal and image processing for clutter suppression. The authors hope that this tutorial has been worthwhile and useful to all those who spent the time reading it.

**Acknowledgment.** Some of the work described in this tutorial paper is related to projects at the University of Arizona funded by L3Harris. However, this paper was prepared as unfunded work (normal University of Arizona duties).

**Disclosures.** The authors declare no conflicts of interest.

**Data Availability.** Data underlying the results presented in this paper are not publicly available at this time but may be obtained from the authors upon reasonable request.

## REFERENCES

1. "Gatwick Airport drone incident," [https://en.wikipedia.org/wiki/Gatwick\\_Airport\\_drone\\_incident#:~:text=On%20the%20evening%20of%2028,Airport%20around%2090%20minutes%20later](https://en.wikipedia.org/wiki/Gatwick_Airport_drone_incident#:~:text=On%20the%20evening%20of%2028,Airport%20around%2090%20minutes%20later).
2. S. Shackle, "The mystery of the Gatwick drone", The Guardian. ISSN 0261-3077. Retrieved 1 December 2020.
3. S. Bray, "Legion Pod achieves major milestones," 2020, <https://www.acc.af.mil/News/Article-Display/Article/2274043/legion-pod-achieves-major-milestones/>.
4. S. Kim and J. Lee, "Small infrared target detection by region-adaptive clutter rejection for sea-based infrared search and track," *Sensors* **14**, 13210–13242 (2014).
5. H. B. Srivastava, Y. B. Limbu, R. Saran, and A. Kumar, "Airborne infrared search and track systems," *Def. Sci. J.* **57**, 739 (2007).
6. S. Kim, Y. Yang, and B. Choi, "Realistic infrared sequence generation by physics-based infrared target modeling for infrared search and track," *Opt. Eng.* **49**, 116401 (2010).
7. M. Everett, D. Manson, A. Brook, and G. Davidson, "A naval infrared search and track demonstrator and its fusion with other ship sensors," *Proc. SPIE* **6206**, 620626 (2006).
8. L. Fortunato, G. Colombi, A. Ondini, C. Quaranta, C. Giunti, B. Sozzi, and G. Balzarotti, "SKYWARD: the next generation airborne infrared search and track," *Proc. SPIE* **9819**, 98190K (2016).
9. G. Gaussorgues and T. Campos, "Low-cost shipborne passive infrared search and track," *Proc. SPIE* **4130**, 577–580 (2000).
10. B. A. Blecha, T. Coty, J. J. Curry, H. T. Graves, R. C. Guckian, J. M. Hall, S. B. McDowell, S. H. Nguyen, R. N. Samuels, T. E. Smith, J. J. Wiedmann, and R. A. Wright, "Second generation FLIR common modules," U.S. patent US5510618A (23 April 1994).
11. R. Driggers, M. Freidman, and J. Nichols, *Introduction to Infrared and Electro-Optical Systems* (Artech House, 2012), Chap. 7.
12. C. Olson, M. Theisen, T. Pace, C. Halford, and R. Driggers, "Model development and system performance optimization for staring infrared search and track (IRST) sensors," *Proc. SPIE* **9820**, 98200B (2016).
13. S. Butrimas, R. G. Driggers, C. Halford, H. Gemar, G. Tener, M. Theisen, C. Olson, and G. Holst, "Pulse visibility factor and its impact on infrared search and track systems," *Opt. Eng.* **58**, 073105 (2019).
14. C. A. Klein, "How infrared missile windows degrade the noise-equivalent irradiance of infrared seeker systems," *Proc. SPIE* **2286**, 458–470 (1994).
15. J. Green and T. Robinson, "Measuring noise equivalent irradiance of a digital short-wave infrared imaging system using a broadband source to simulate the night spectrum," *Proc. SPIE* **9452**, 945207 (2015).
16. C. A. Klein, "Thermal imaging performance of passive infrared scanners," *IEEE Trans. Geosci. Electron.* **9**, 139–146 (1971).
17. J. Communal, "Comparing camera sensitivity with noise equivalent irradiance," *6th Workshop on Hyperspectral Image and Signal Processing: Evolution in Remote Sensing (WHISPERS)*, Lausanne, Switzerland, 2014, pp. 1–4.
18. D. Ting, S. Rafol, S. Keo, J. Nguyen, A. Khoshakhlagh, A. Soibel, L. Hoglund, A. Fisher, E. Luong, J. Mumolo, J. Liu, and S. Gunapala, "InAs/InAsSb Type-II superlattice mid-wavelength infrared focal plane array with significantly higher operating temperature than InSb," *IEEE Photon. J.* **10**, 6804106 (2018).
19. K. G. Gilbert, L. J. Otten, and W. C. Rose, "Aerodynamic heating," in *Atmospheric Propagation of Radiation*, F. G. Smith, ed., Vol. 2 of The Infrared & Electro-Optical Systems Handbook (Infrared Information Analysis Center/SPIE, 1993), p. 240.
20. J. Liu, H. Yue, J. Lin, and Y. Zhang, "A simulation method of aircraft infrared signature measurement with subscale models," *Procedia Comput. Sci.* **147**, 2–16 (2019).
21. N. Fudala, R. Short, J. Hewitt, C. Halford, T. Pace, D. Manville, M. Theisen, C. Fearing, A. Dapore, C. Olson, G. Tener, D. Gaudiosi, K. Richardson, and R. Driggers, "Comparison of midwave versus longwave intensity signatures for infrared search and track of small rotorcraft unmanned aerial vehicles," *Opt. Eng.* **58**, 043107 (2019).
22. M. Theisen, C. Olson, G. Buritica, A. Sarto, G. Tener, R. Driggers, C. Halford, and D. Shelton, "A comparison of MWIR and LWIR staring long range infrared search and track (IRST) performance," in *Military Sensing Symposium* (National Institutes of Standards and Technology, 2016).
23. R. G. Driggers, C. E. Halford, M. J. Theisen, D. M. Gaudiosi, S. C. Olson, and G. D. Tener, "Staring array infrared search and track performance with dither and stare step," *Opt. Eng.* **57**, 053101 (2018).
24. R. Driggers, C. Halford, M. Theisen, D. Gaudiosi, C. Olson, G. Tener, and T. Pace, "Staring array versus scanning infrared search and track (IRST) performance," in *Military Sensing Symposium* (National Institutes of Standards and Technology, 2018).